Current Science
CS 5 (4), 3443-3465 (2025)
Received 12 April 2025 | **Revised** 08 May 2025 | **Accepted** 14 June. 2025 | **Online Available** 03 July 2025
https://doi.org/ 10.52845/CS/2025-5-4-10

Current Science
Current Science

OPEN ACCESS **ISSN(O)2795-8639**

Original Article

Fine Zoning of Axial Flow Kaplan Turbine Operating Regions Based on Pressure Pulsation Visualization Tracking

Mingkun Fang[1], Houyu Zhang[2], Yunshui Peng[3], Jinfu Lin[3], Yingbo Guan[2], Ran Tao[1,4], Di Zhu[5], Ruofu Xiao[1,4,a]

[1]College of Water Resources and Civil Engineering, China Agricultural University, Beijing, 100083, China

[2]State Grid Fujian Electric Power Research Institute, Fuzhou, 350007, Fujian Province, China

[3]Fujian Shuikou Power Generation Group Co., Ltd., Fuzhou, 350004, China

[4]Beijing Engineering Research Center of Safety and Energy Saving Technology for Water Supply Network System, China Agricultural University, Beijing 100083, China

[5]College of Engineering, China Agricultural University, Beijing, 100083, China

[*]Corresponding Author: Ruofu Xiao

Abstract:
Under the global context of energy transition and sustainable development, enhancing the operational efficiency of hydraulic turbines and reducing energy losses are significant for the hydropower industry. This study, based on entropy generation theory and pressure fluctuation tracking network methodology, combines numerical simulations with experimental research to thoroughly investigate the energy characteristics and operational features of Kaplan turbines under different guide vane and runner blade matching conditions. Additionally, a Turbine Operating Zone Density Clustering Algorithm (TOZ-DBSCAN) is proposed for operational condition point classification in Kaplan turbines. The following results and conclusions were drawn: The energy loss within the draft tube is the primary cause of efficiency decline in hydraulic turbines. The internal pressure fluctuation intensity of the turbine is highest when the runner blade is at 0°. When the blade opening is at -5°, the overall entropy generation of the unit remains relatively stable, with lower energy losses. The maximum entropy generation in the H3 (High-head 3) operational condition is relatively high. The TOZ-DBSCAN method effectively identifies "inferior" operational condition points characterized by low efficiency and high fluctuations. The findings of this study provide theoretical support for the stable operation and efficient regulation of hydraulic turbines.

Keywords: Axial flow Kaplan turbine, Entropy generation, Pressure pulsation, machine learning, guide vane and runner blade matching

1. Introduction

With the continuous growth of the global economy, particularly the industrialization and energy transition processes in developing countries and emerging markets, energy demand continues to rise.[1-3] With the introduction of carbon peak and carbon neutrality goals,[4] there is a pressing need to further promote renewable energy sources, such as wind, solar, hydro, and nuclear power, to reduce reliance on fossil fuels and drive the transition of the energy structure from traditional coal and oil to cleaner and low-carbon energy sources.[5,6] Hydropower, as a significant renewable energy source, has become a major contributor to global electricity production.[7] According to data from the International Energy Agency (IEA) in 2021, hydropower accounts for 16% of global electricity production and is the most important component of renewable energy electricity generation worldwide. The global installed capacity of hydropower is approximately 1,300 GW, with about half of this capacity located in China.[8,9] The electricity generation of hydropower plants is closely related to water flow, and seasonal and climatic changes can lead to uncertainties in water flow. This necessitates flexible dispatch capabilities for hydropower plants to ensure stable electricity generation even during periods of low water flow.

The Kaplan turbine is a type of hydroelectric generator that directly utilizes water flow to act on the runner blades, is typically employed in hydropower stations characterized by low head and high flow rates, making it particularly suitable for large-scale hydroelectric power plants.[10,11] The guide vane and runner blade matching in Kaplan turbines is one of the critical factors influencing their performance and efficiency.[12,13] After passing through the guide vanes, the water flow enters the runner blades, and the matching relationship between the guide vanes and runner blades determines the flow characteristics such as velocity, pressure, and angle, which in turn affect the turbine's operational efficiency and pressure fluctuation performance during operation.[14] An improper matching relationship between the guide vane angle and the runner blade angle can lead to increased energy losses and pressure fluctuations within the unit,[15] manifesting as a decline in the turbine's efficiency. Therefore, the operational efficiency and stability of Kaplan turbines are crucial factors in ensuring the continuous, stable, and efficient power generation of hydropower stations, directly impacting power generation capacity, energy utilization efficiency, equipment maintenance costs, and the overall economic performance of the hydropower plant.[16] During operation, it is essential to consider the spatial propagation characteristics of pressure fluctuations and the patterns of energy loss, employing advanced visualization analysis techniques and optimization algorithms to delineate operational regions.

In the field of pressure fluctuation research in hydraulic turbines, Yang et al.[17] utilized the realizable K-Epsilon model and polyhedral mesh method to investigate the pressure fluctuation characteristics of a horizontal-axis twin-runner Francis turbine. They analyzed the mutual influence between the two runners, and the results indicated that the presence of vortex zones leads to uneven pressure distribution at the runner outlet, which is a significant factor causing flow asymmetry within the runner. Wang et al.[18] studied the high-amplitude pressure fluctuations induced by complex internal flows in a pump-as-turbine (PAT). Their findings suggested that mixed-flow PATs are more suitable for operation under flow conditions of 0.7q and 0.8q. Yang et al.[19] investigated the evolution characteristics of pressure fluctuations in the dustpan-shaped conduit of an axial-flow PAT. By comparing simulated pressure fluctuation signals with model test results, they concluded that as the distance from the impeller increases, the dominant frequency of pressure pulsation shifts from 3 times the rotational frequency to 0.5 times the rotational frequency. He et al.[20] examined the pressure fluctuation characteristics inside the draft tube of a pump-turbine, explaining the pressure fluctuation patterns from the perspective of water column separation. Their study revealed that during the transition process, the pressure fluctuation amplitude is highest during water column bridging, reaching up to 4.18 m at small openings. Liu et al.[21] conducted an in-depth analysis of the pressure fluctuation characteristics of a Kaplan turbine under three different heads. Zhang et al.[22] reduced the pressure fluctuation intensity in the draft tube by optimizing the trailing edge shape of the runner blades. He et al.[23] investigated the pressure fluctuations caused by rapid guide vane closure and the water column separation phenomenon induced by water hammer superposition. Existing research primarily focuses on the impact of single factors on turbine pressure fluctuations, with relatively limited studies on the division and optimization of operational regions for different Kaplan turbines, such as the delineation of high-efficiency zones, low-efficiency zones, and unstable regions.

As an important branch of machine learning, deep learning has seen significant development and application in recent years, with its use in the field of hydraulic turbine operation gradually increasing. Roh et al.[24] employed deep learning algorithms to predict the rotational speed of the turbine generator in an oscillating water column-type wave energy converter (OWC-WEC). The results demonstrated that LSTM exhibits the most accurate prediction of the instantaneous rotational speed of a turbine generator, while CNN has visible advantages when data correlation is low. Liu et al.[25] proposed a deep forest-based end-to-end intelligent fault diagnosis method for hydraulic turbines, validating the effectiveness of the proposed method using experimental datasets under twelve conditions. The results showed that the proposed method has advantages in both diagnostic accuracy and robustness. Pan et al.[26] proposed an IPSO-LSTM-based refinement method for fitting the turbine flow characteristic curve using deep learning methods. The results indicated that this model can effectively improve the accuracy of fitting and predicting turbine flow characteristics. Xu et al.[27] introduced an innovative deep learning-based fluid-structure interaction model. Xiong et al.[28] proposed a universal, fast, and memory-efficient method for time-series prediction of hydraulic turbines. Korkps et al.[29] demonstrated that the features extracted by the deep autoencoder are more informative than those extracted by PCA and kernel PCA. Masood et al.[30] proposed a machine learning-based surrogate model for accelerating simulation-driven optimization of hydropower Kaplan turbines. Although the application of deep learning in hydraulic turbine operation research has gradually increased, there remains a research gap in the clustering analysis of operational condition points and the division of operational regions using deep learning. Therefore, there is a need to utilize deep learning methods for clustering analysis of turbine operational points.

In this study, numerical simulations were conducted on ten typical operational condition points of a Kaplan turbine. The analysis focused on the percentage of pressure fluctuations, entropy generation distribution at different draft tube locations, and the spatial propagation patterns of pressure fluctuations. The Turbine Operating Zone Density Clustering Algorithm (TOZ-DBSCAN) was employed to classify the operational condition points of the turbine. The aim of this research is to propose a dynamic turbine operational region division method based on pressure fluctuation visualization tracking, which comprehensively considers entropy generation distribution and pressure fluctuation propagation patterns. This method aims to accurately identify abnormal operational states and high energy loss regions, thereby providing a scientific basis for optimizing turbine operation strategies. Figure 1 illustrates the main research framework of this study. In subsequent chapters, the operational characteristics under different guide vane and runner blade combinations will be systematically discussed from two perspectives: pressure fluctuations and energy dissipation. By integrating the analysis results of both aspects, the dynamic turbine operational region division results based on pressure fluctuation visualization tracking will be ultimately derived.

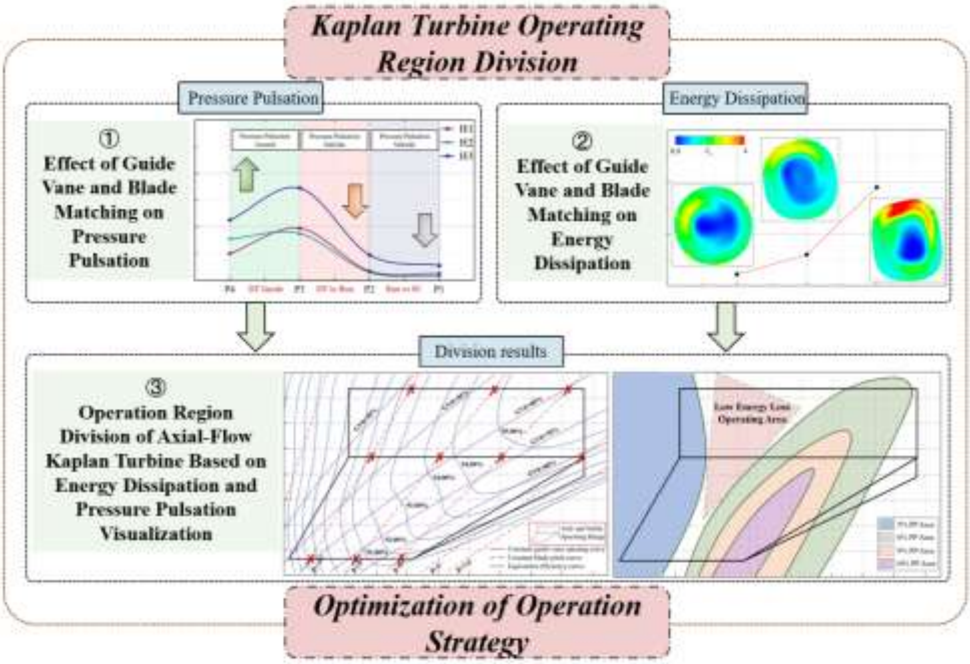

Figure 1: Research Framework of the Paper

2 Research Object and Grid Division

2.1Fluid Domain Model of Axial-Flow Kaplan Turbine

The subject of this study is a Kaplan turbine, with the hydropower station designed for a total installed capacity of 1400 MW and a guaranteed output of 230 MW per unit. The full flow passage of the Kaplan turbine was modeled using UG NX software. The model consists of five main components, arranged in the order of water flow: the spiral casing, fixed guide vanes, movable guide vanes, runner, and draft tube. The overall computational model is illustrated in Figure 2. The number of fixed guide vanes and movable guide vanes is 24 each, and the runner has 6 blades. The inlet is defined as a pressure inlet, and the outlet as a pressure outlet, with the head simulated by the pressure difference between the inlet and outlet.

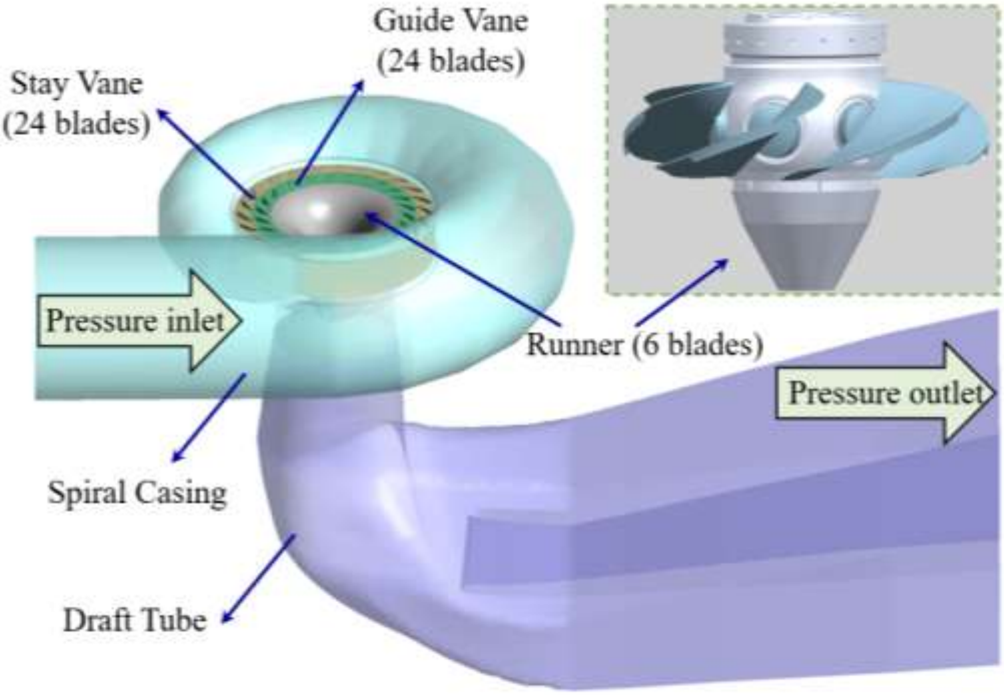

Figure 2: Three-dimensional model of an axial-flow Kaplan turbine

2.2 Grid Division and Independence Verification

Given the complex geometry of the Kaplan turbine, unstructured meshes, which offer better adaptability to boundaries, were selected for meshing the model. The meshing results are shown in Figure 3.

In the numerical simulation process, the quality of the mesh directly affects the accuracy of the computational results. Overly coarse meshes can lead to non-convergence and compromise the accuracy of the results, while overly refined meshes, although beneficial for improving computational stability and precision, can also consume excessive computational resources. The Grid Convergence Index (GCI) is a commonly used method for mesh independence verification, employed to assess the convergence of numerical solutions with respect to mesh refinement.[31] By progressively refining the mesh and checking the convergence of the computational results, the adequacy of the mesh refinement can be validated. In this study, the unit output was selected as the key control variable for mesh independence verification. Three mesh schemes were considered, with mesh counts of M1=4,083,239, M2=9,227,300, and M3=15,792,379, respectively. Figure 4 presents the results of the mesh independence verification, showing the computed unit output values and the Richardson extrapolation values for the three mesh schemes under the condition of infinitely dense meshes. The GCI values between the coarse mesh and the medium-density mesh, as well as between the medium-density mesh and the fine mesh, were 0.089% and 0.032%, respectively, both satisfying the convergence criteria. Consequently, the medium-density mesh M2 was selected as the computational mesh for subsequent steady and unsteady calculations.

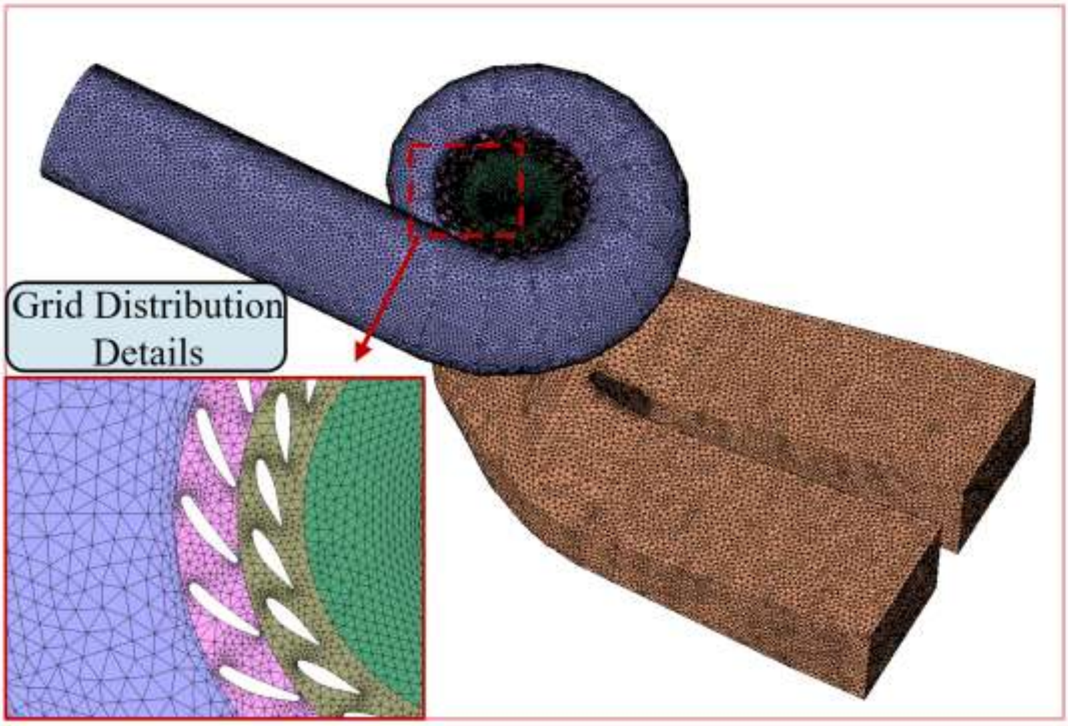

Figure 3: Fluid domain computational mesh distribution

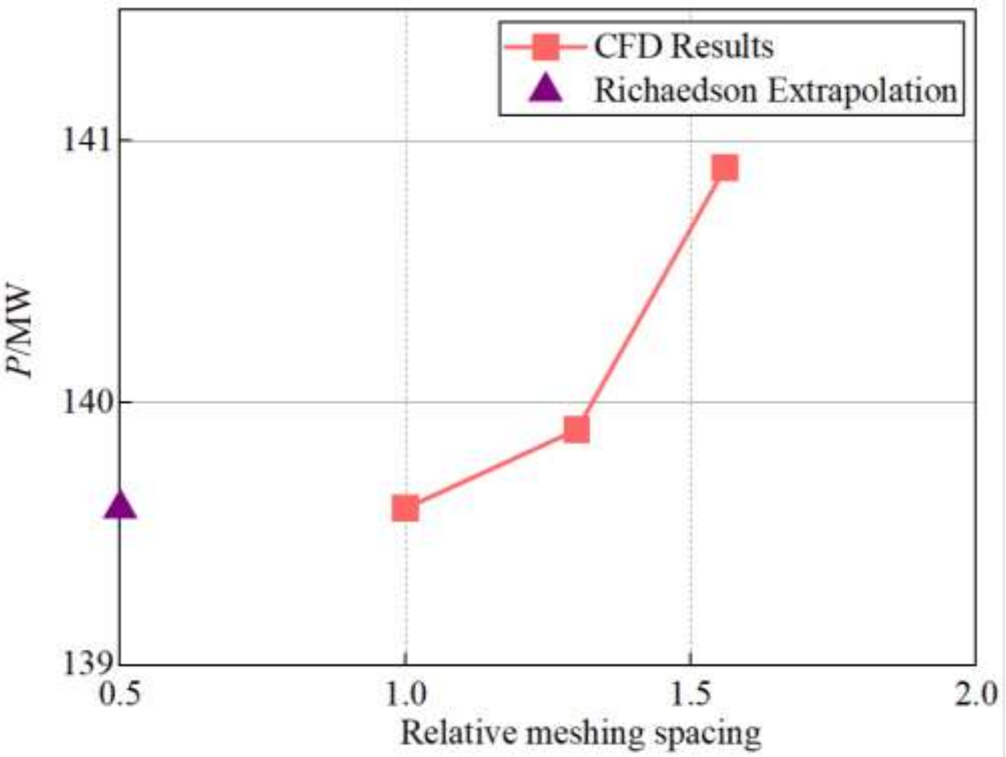

Figure 4: Grid independence verification results

3 Research Method

3.1 CFD Control Equations and Turbulence Models

The governing equations of computational fluid dynamics (CFD) are based on the fundamental principles of fluid mechanics, mathematically describing the motion and interactions of fluids. These include the continuity equation, the momentum equation, and the energy equation. For the scope of this study, the temperature variations within the turbine can be neglected, and thus the energy equation is not considered in the numerical simulations. The continuity equation and momentum equation are expressed as follows:

$$\frac{\partial \rho}{\partial t}+\frac{\partial(\rho v_x)}{\partial x}+\frac{\partial(\rho v_y)}{\partial y}+\frac{\partial(\rho v_z)}{\partial z}=0 \quad (1)$$

where, ρ is density of the fluid medium; t is time; v_x, v_y and v_z are the components of velocity vector in the X, Y and Z directions respectively.

$$\frac{\partial(\rho v)}{\partial t}+(\rho v\cdot\nabla)v=-\nabla p+\mu\nabla^2 v+\rho f \quad (2)$$

where, μ is dynamic viscosity coefficient of fluid, v is velocity vector, ∇ is Hamiltonian operator, and f is stress vector.

Selecting an appropriate turbulence model is crucial for accurately capturing the complex flow characteristics and energy propagation within hydraulic turbines. In this study, the SST (Shear-Stress Transport) k-ω model is chosen for numerical simulations. This model, proposed by Menter as an improvement over the standard k-ω model, combines the advantages of the k-ε and k-ω models, making it widely applicable in engineering and scientific research. The SST k-ω model employs the k-ω model in the near-wall region, the k-ε model in the free-stream region, and a blending function F_1 to achieve a smooth transition between the two models in the intermediate region. This characteristic enables the SST k-ω model to provide high-precision flow field calculations both near the wall and in the free-stream regions. The governing equations of the model are as follows:[32,33]

The eddy viscosity limit equation is:

$$v=\frac{a_1 k}{\max\left(a_1\omega, SF_2\right)} \quad (3)$$

The mixed function expression is as follows:

$$F_1=\tanh\left(\min\left(\max\left(\frac{\sqrt{k}}{\beta^*\omega y},\frac{500v}{y^2\omega}\right),\frac{4\rho k}{CD_{k\omega}\sigma_{\omega 2}y^2}\right)^4\right) \quad (4)$$

$$CD_{k\omega}=\max\left(2\rho\frac{1}{\sigma_{\omega 2}\omega}\frac{\partial k}{\partial x_j}\frac{\partial \omega}{\partial x_j},1.0\times 10^{-10}\right) \quad (5)$$

$$F_2=\tanh\left(\left(\max\left(\frac{2\sqrt{k}}{\beta^*\omega y},\frac{500v}{y^2\omega}\right)\right)^2\right) \quad (6)$$

where y is the closest distance to the wall, v is the kinematic viscosity, k is turbulent kinetic energy and ω is dissipation rate of specific energy. β^* is the empirical coefficient, typically set to a value of 0.09, and a specific value of $\sigma_{\omega 2}$, which is 0.856. This model exhibits k-ω behavior near the wall, with F_1 equal to 1. As the distance from the wall increases, the model transitions into a k-ε

mode, where F_1 becomes 0.

3.2 Entropy Production Theory

Entropy generation is a quantity that describes the intensity of irreversible processes within a system. By analyzing the entropy generation distribution across flow cross-sections, regions with significant energy dissipation in the internal flow of a Kaplan turbine can be visually identified. This provides valuable insights for the division of operational regions and the adjustment of operational condition points in Kaplan turbines.

Among the factors contributing to entropy generation, the dissipation effect (SPD) and the heat transfer effect (SPC) are critical parameters for describing energy losses and heat transfer within the system. SPD and SPC can be further divided into two components: the viscous dissipation term (mean term) and the turbulent dissipation term (fluctuating term). The definitions of SPD and SPD′ are as follows:

$$S_{P\bar{D}} = \frac{\mu}{\bar{T}}\left[2\left\{\left(\frac{\partial \bar{u}}{\partial x}\right)^2 + \left(\frac{\partial \bar{v}}{\partial y}\right)^2 + \left(\frac{\partial \bar{w}}{\partial z}\right)^2\right\} + \left(\frac{\partial \bar{u}}{\partial y} + \frac{\partial \bar{v}}{\partial x}\right)^2 + \left(\frac{\partial \bar{u}}{\partial z} + \frac{\partial \bar{w}}{\partial x}\right)^2 + \left(\frac{\partial \bar{v}}{\partial z} + \frac{\partial \bar{w}}{\partial y}\right)^2\right] \tag{7}$$

$$S_{PD'} = \frac{\mu}{T'}\left[2\left\{\left(\frac{\partial u'}{\partial x}\right)^2 + \left(\frac{\partial v'}{\partial y}\right)^2 + \left(\frac{\partial w'}{\partial z}\right)^2\right\} + \left(\frac{\partial u'}{\partial y} + \frac{\partial v'}{\partial x}\right)^2 + \left(\frac{\partial u'}{\partial z} + \frac{\partial w'}{\partial x}\right)^2 + \left(\frac{\partial v'}{\partial z} + \frac{\partial w'}{\partial y}\right)^2\right] \tag{8}$$

$S_{P\bar{C}}$ and $S_{PC'}$ are the viscous dissipation term (mean term) and the turbulent dissipation term (fluctuation term) of the heat transfer effect, which can be expressed as:

$$S_{P\bar{C}} = \frac{\lambda_t}{T^2}\left[\left(\frac{\partial \bar{T}}{\partial x}\right)^2 + \left(\frac{\partial \bar{T}}{\partial y}\right)^2 + \left(\frac{\partial \bar{T}}{\partial z}\right)^2\right] \tag{9}$$

$$S_{PC'} = \frac{\lambda_t}{T^2}\left[\overline{\left(\frac{\partial T'}{\partial x}\right)^2} + \overline{\left(\frac{\partial T'}{\partial y}\right)^2} + \overline{\left(\frac{\partial T'}{\partial z}\right)^2}\right] \tag{10}$$

In order to effectively characterize the irreversible energy loss in the flow and evaluate the energy loss characteristics of turbine operating conditions, the local entropy production rate (E_{pro}) induced by velocity fluctuations is visualized and analyzed to assess flow energy dissipation. Its formula is defined as follows:

$$E_{pro} = \beta \frac{\rho \omega k}{T} \tag{11}$$

The meanings of the parameters in the above formula are as follows: β is an empirical constant in the turbulence model, with a specific value of 0.09. k represents turbulent kinetic energy, ω denotes the turbulent eddy frequency, and T represents temperature.

3.3 Visualization Method for Pressure Pulsation Tracking Network (PTN)

Traditional pressure pulsation monitoring points can only obtain time-series data of pressure signals at the monitored points, revealing the amplitude and frequency characteristics of pressure pulsations at specific locations. However, they cannot capture the propagation process of pressure pulsations at these locations. Compared to conventional pressure pulsation analysis methods, the visualization-based PTN method enables monitoring of the dominant frequency distribution of pressure pulsations on specific turbine planes. It also analyzes the amplitude and phase propagation of pressure pulsations under the corresponding dominant frequency distribution, effectively identifying the propagation and attenuation patterns of pressure pulsations on a given plane. By deploying multiple PTN monitoring planes, the pressure pulsation propagation patterns within the entire turbine unit can be further obtained.

This study adopts a combined point-plane analysis approach. First, pressure pulsation monitoring points are set at key locations of the unit's operation to analyze the percentage variation patterns of pressure pulsations at different positions based on monitoring results. Specifically, P1 is in the volute, P2 in the runner domain, and P3 and P4 in the draft tube. For the layout of the visualization-based PTN planes, the focus is on the draft tube region, where pressure pulsations are relatively strong. PTN monitoring planes are set at three positions: Z = -10 m, Z = -12 m, and Z = -14 m, with each plane containing 966 pressure pulsation monitoring points. By analyzing the propagation patterns of pressure pulsations across different planes, the propagation characteristics of pressure pulsations in the draft tube under different operating conditions can be obtained. The locations of individual monitoring points (P1-P4) and the three monitoring planes are shown in the sectional view of the unit, as illustrated in Figure 5.

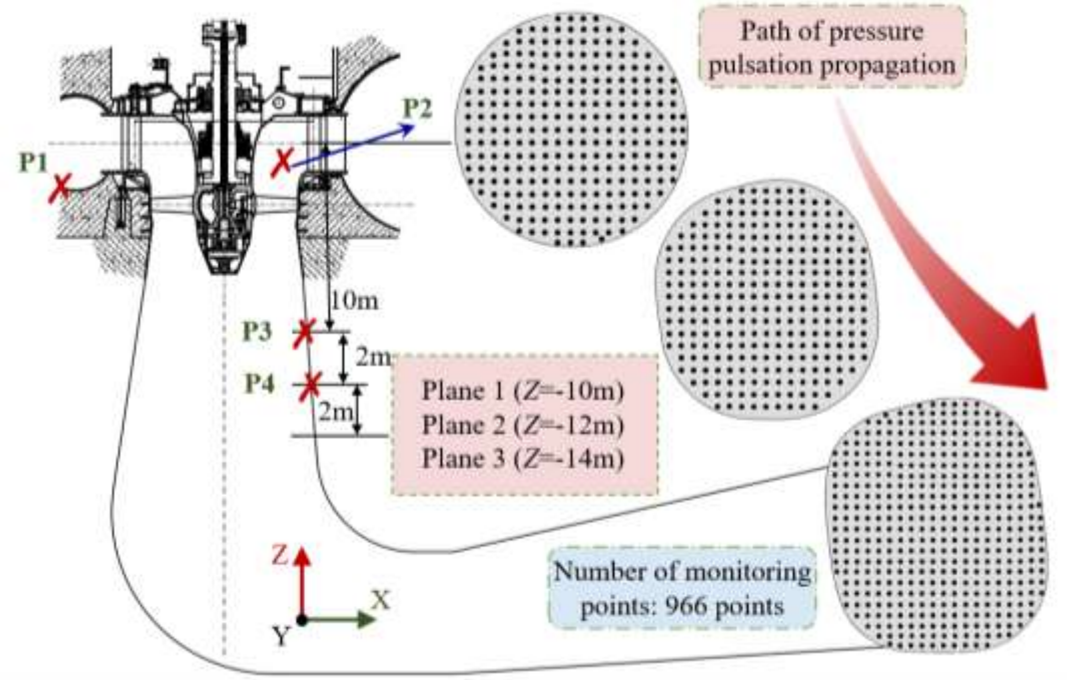

Figure 5: Pressure pulsation data monitoring system

3.4 Distribution of Operating Condition Points in the Operating Area

The expected operational characteristic curve of the turbine studied in this paper is shown in Figure 6, and the main parameters of the turbine are listed in Table 1. In Figure 6, the horizontal axis represents the unit output power *P* (MW), while the vertical axis represents the effective net head H_{net} (m). The figure includes constant blade opening curves and constant guide vane opening curves. The intersection points or interpolated points of these curves represent operating points, corresponding to specific guide vane and blade combinations. By calculating different guide vane and blade combination conditions, this study investigates the influence of their dynamic matching on the propagation of pressure pulsations and energy dissipation patterns in the unit. To ensure a comprehensive evaluation of the turbine's operational characteristics, numerical simulation operating points are arranged within the safe and efficient operating range of the unit, ensuring coverage of the full operating range while accurately reflecting its performance. Specifically, three calculation points are selected in the high-head range, denoted as H1 (High-head 1)–H3 (High-head 3). Since the medium-head range covers a broader operational region, four calculation points are selected under this condition, denoted as M1 (Mid-head 1)–M4 (Mid-head 4). In the low-head range, three calculation points are chosen, denoted as L1 (Low-head 1)–L3 (Low-head 3).

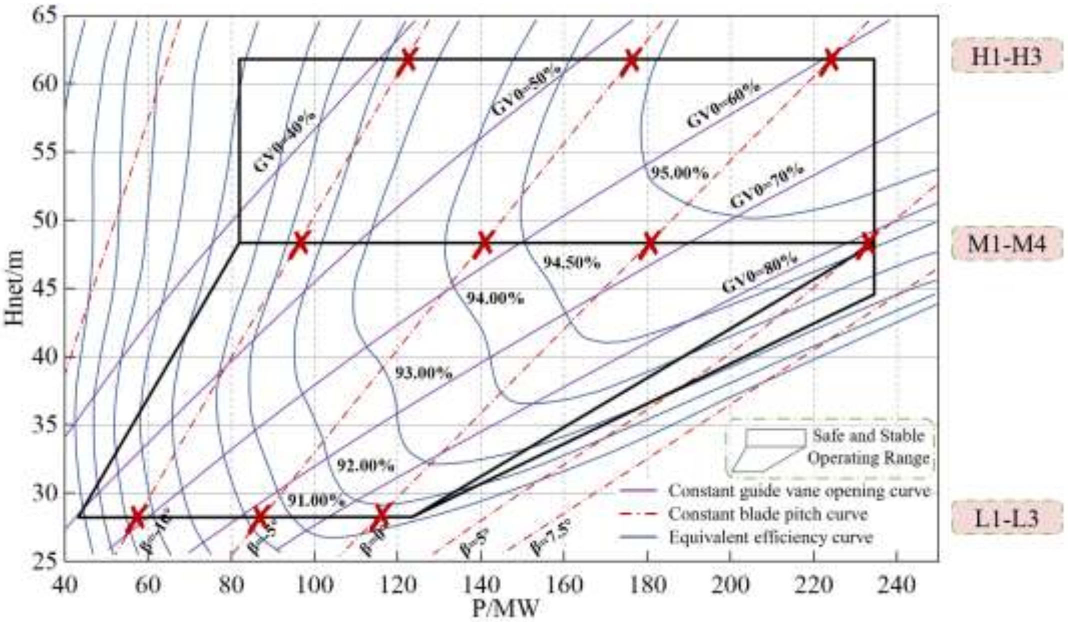

Figure 6: Expected operating characteristic curve of Kaplan turbine

Table 1: Main parameters of Kaplan turbine.

Parameter	Symbol	Value	Unit
Outlet diameter of runner	D_2	2.238	m
Rated output	P	230	MW
Rotating speed	n_s	107.1	r/min
Number of runner blades	Z_r	6	[-]
Number of guide vane blades	Z_G	24	[-]
Rated Head	H_n	48	m
Maximum Head	H_max	62	m
Minimum Head	H_min	28	m

3.5 Turbine Operating Zone Density Clustering Algorithm

This paper considering the characteristics of the turbine operating region, improves the traditional density-based clustering algorithm and proposes a turbine operating region density clustering algorithm. By comprehensively considering two key operational indicators—pressure pulsation and unit efficiency—the proposed algorithm efficiently classifies turbine operating conditions. The specific calculation steps are as follows:

To eliminate the influence of different feature scales, all pressure pulsation data and unit efficiency data are first normalized:

$$X_{\mathrm{norm}} = \frac{X - \mu_X}{\sigma_X} \tag{12}$$

$$Y_{\mathrm{norm}} = \frac{Y - \mu_Y}{\sigma_Y} \tag{13}$$

Calculate the Euclidean distance between each data point to measure the similarity of different operating points, while considering the pressure pulsation amplitude and unit efficiency as key features of the turbine operating state:

$$d(X_i, X_j) = \sqrt{(X_{i1} - X_{j1})^2 + (X_{i2} - X_{j2})^2} \tag{14}$$

Select an appropriate ϵ as the minimum neighborhood distance, which is dynamically determined by calculating the average distance of the k+1th nearest neighbor. Then, define the core point MinPts:

$$\epsilon = \frac{1}{n}\sum_{i=1}^{n} d(X_i, X_k) \tag{15}$$

$$|\{X_j : d(X_i, X_j) \leq \epsilon\}| \geq MinPt \tag{16}$$

Where k is the selected number of nearest neighbors, X_i is the core point, and X_j represents the points within its neighborhood.

4 Result Analysis

4.1 Hydraulic Performance Verification at Operating Points

Before analyzing the specific results, the numerical calculation accuracy needs to be verified. Two points, M3 at medium head and H3 at high head, are selected for this verification, with turbine efficiency as the validation index. The comparison results are shown in Figure 7. By comparing the calculated efficiency with the experimental efficiency at both operating conditions, it is found that the calculated efficiency matches well with the experimental efficiency for both conditions, with errors within 1%. This satisfies the required calculation accuracy, allowing for the subsequent analysis of pressure pulsations and entropy generation characteristics.

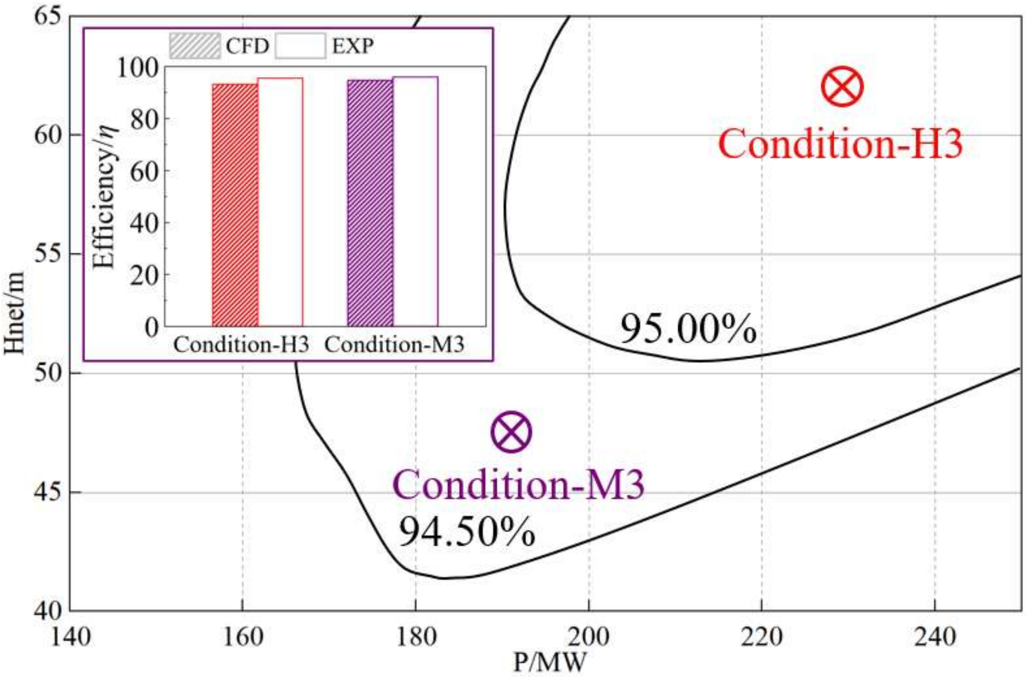

Figure 7: Accuracy verification of numerical simulation Comparison of changes in entropy production distribution along the flow direction under the same operating conditions

4.2 Analysis of Energy Loss in Key Positions

The energy loss characteristics of the unit during operation under different guide vane-blade combinations are primarily studied using two analysis methods: pressure pulsation percentage and entropy generation. These two indicators can reveal the degree of energy loss from different perspectives.

Firstly, the variation pattern of the pressure pulsation percentage at a single point is analyzed. The pressure pulsation percentage can characterize the pulsation intensity at that point during the unit's operation. This value is represented as ΔP*, where ΔP is the peak-to-peak pressure pulsation at the point, and Pout is the average pressure at the turbine outlet cross-section, which serves as the reference pressure. Figures 8(a)-(c) show the variation patterns of pressure pulsation percentage at different operating points under various head conditions. From the figures, several characteristic patterns of the pressure pulsation intensity distribution within the turbine can be observed:

(1) Against the direction of flow inside the turbine, the pressure pulsation percentage shows a trend of first increasing and then decreasing. From P4 to P3, the pressure pulsation intensity increases, and from P3 to P2, the pressure pulsation intensity rapidly weakens. In the region from P2 to P1, the pressure pulsation intensity further decreases and tends to stabilize. Near the monitoring point P3, the pressure pulsation reaches its peak, and the pressure pulsation percentage at P4 is only lower than at P3. This indicates that the energy loss in the turbine's draft tube is relatively significant and is the main reason affecting the turbine's operational efficiency.

(2) Under the same head conditions, there are also differences in the variation range of the pressure pulsation percentage between different operating points. Under low head conditions, the L3 condition (blade 0°-guide vane 37°) has a higher pressure pulsation percentage at various positions in the turbine compared to the other two conditions, while the pressure pulsation intensity under the L1 condition remains at a relatively low level. Similar patterns are observed under medium and high head conditions, where the M3 and H3 conditions show relatively higher pressure pulsation intensities under their respective head conditions. The increase in pressure pulsation intensity is notably higher compared to the different operating conditions at the same head.

(3) The overall pressure pulsation intensity at low head remains at a relatively high level, while at high head, it is maintained at a lower level. By correlating the analysis results with the blade-guide vane combinations, it is found that at a blade angle of 0°, the pressure pulsation intensity inside the turbine is higher, while at a blade angle of -5°, the overall pressure pulsation intensity of the turbine is lower. This analysis provides a reference for the subsequent analysis of the spatial propagation law of pressure pulsations.

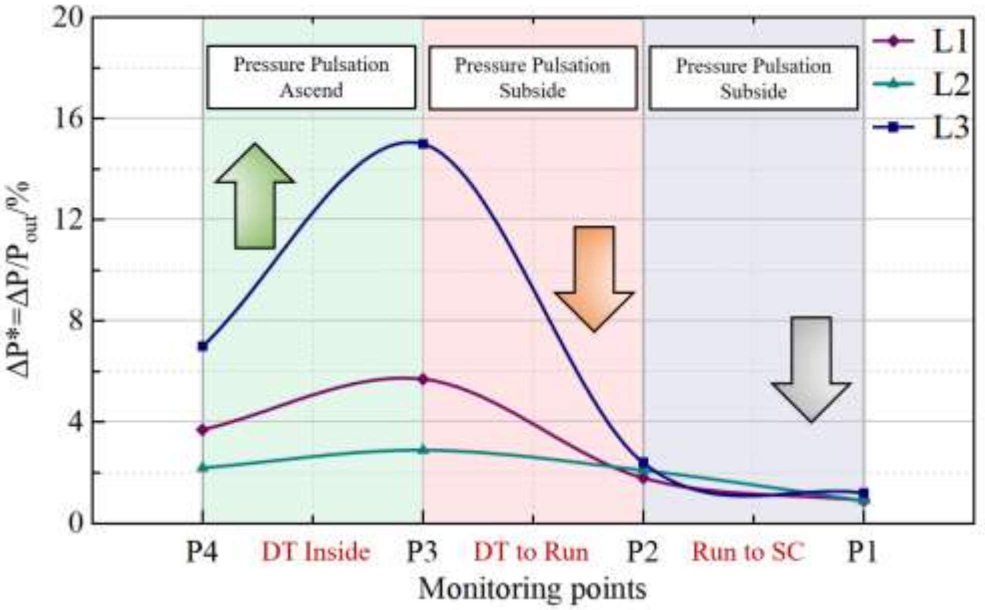

(a) The percentage variation law of pressure pulsation in low head L1-L3

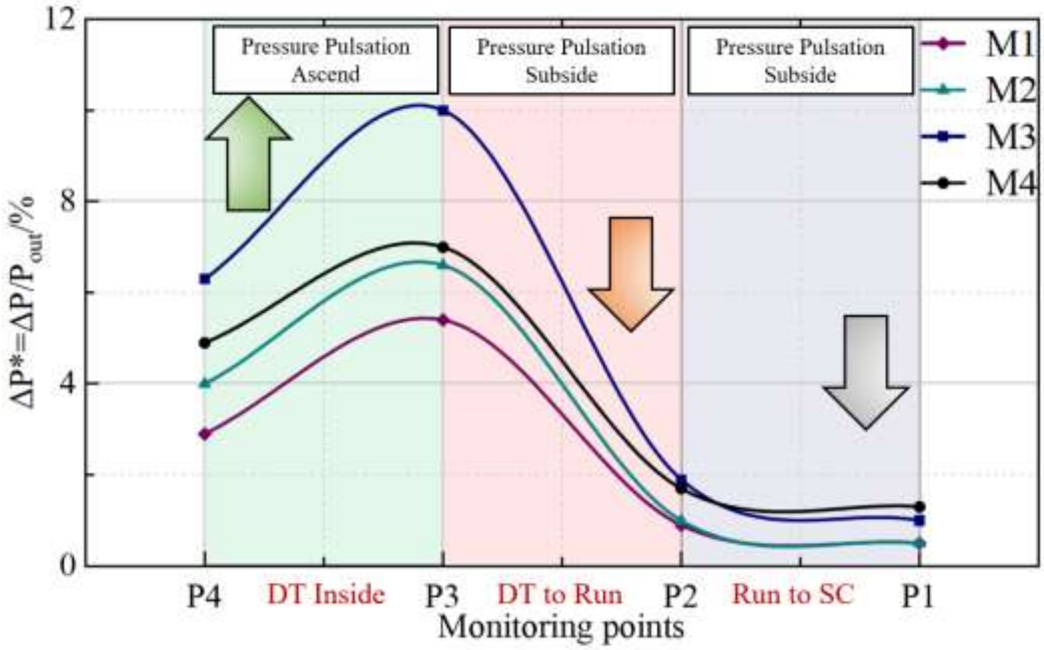

(b): The percentage variation law of pressure pulsation in medium head M1-M4

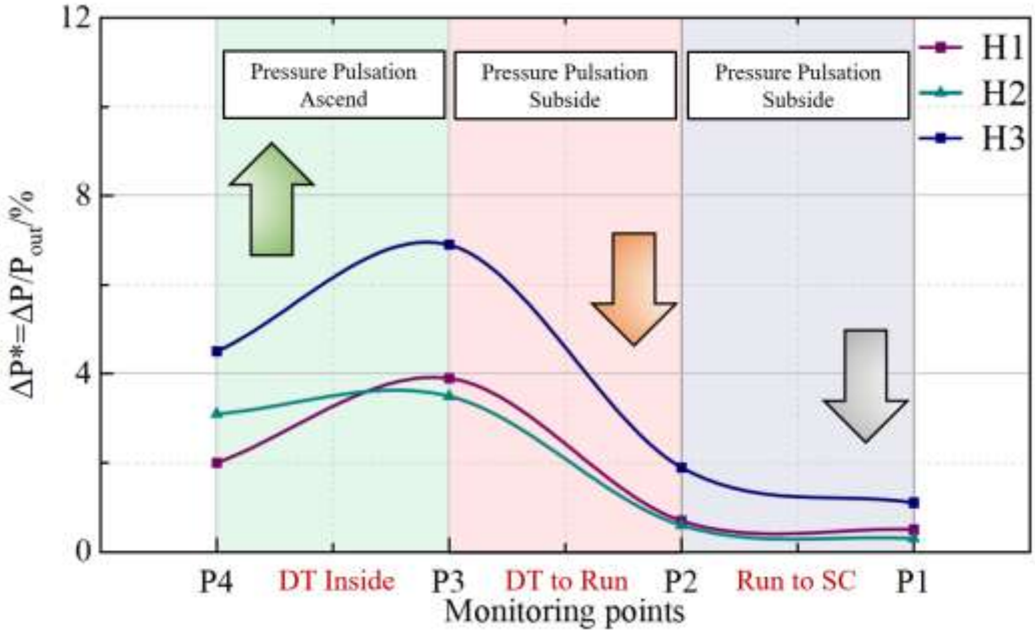

(c): The percentage variation law of pressure pulsation in high head H1-H3

Figure 8: Percentage variation of pressure pulsation at different operating points under different heads

The pressure pulsation percentage can characterize the instability of the flow field and its energy loss, mainly reflecting the amplitude variation of fluid pressure pulsations. However, it cannot quantitatively assess the energy loss state at a specific flow position. Therefore, by utilizing entropy generation analysis, a more comprehensive understanding of the energy dissipation sources and distribution patterns caused by flow instability can be achieved. In this study, the entropy generation analysis of different flow sections in the draft tube is divided into quantitative and qualitative analyses. Through quantitative analysis, operating conditions with higher energy dissipation are identified, which are then further analyzed qualitatively. Figure 9 shows the distribution patterns of the maximum and minimum values of E_p at three monitoring planes under different operating conditions. From the figure, it can be observed that the fluctuation amplitude of entropy generation is significant under different operating conditions, and there are marked local variations in energy loss within the same plane. By comparing the maximum values of E_p, it is found that under different head conditions, the L2, M2, and H2 operating conditions correspond to the minimum entropy generation values for the respective head conditions. This indicates that when the turbine operates with a blade angle of -5°, the overall entropy generation of the unit is relatively stable, with lower energy loss. By comparing the entropy generation variation patterns between different planes, it is observed that the energy dissipation degree gradually increases in the direction of flow. In Plane 3, except for the H2 condition, the maximum Ep values for other conditions exceed 4, and the scale of entropy generation significantly increases compared to the first two flow planes. The maximum entropy generation value for the H3 operating condition is relatively high. Therefore, based on the quantitative analysis, a visualized analysis of the entropy generation distribution in the corresponding sections during the operation of L3, M3, and H3 (with a blade angle of 0°) is performed, further clarifying the location of high entropy generation areas and providing a basis for accurately delineating the operational regions of the turbine.

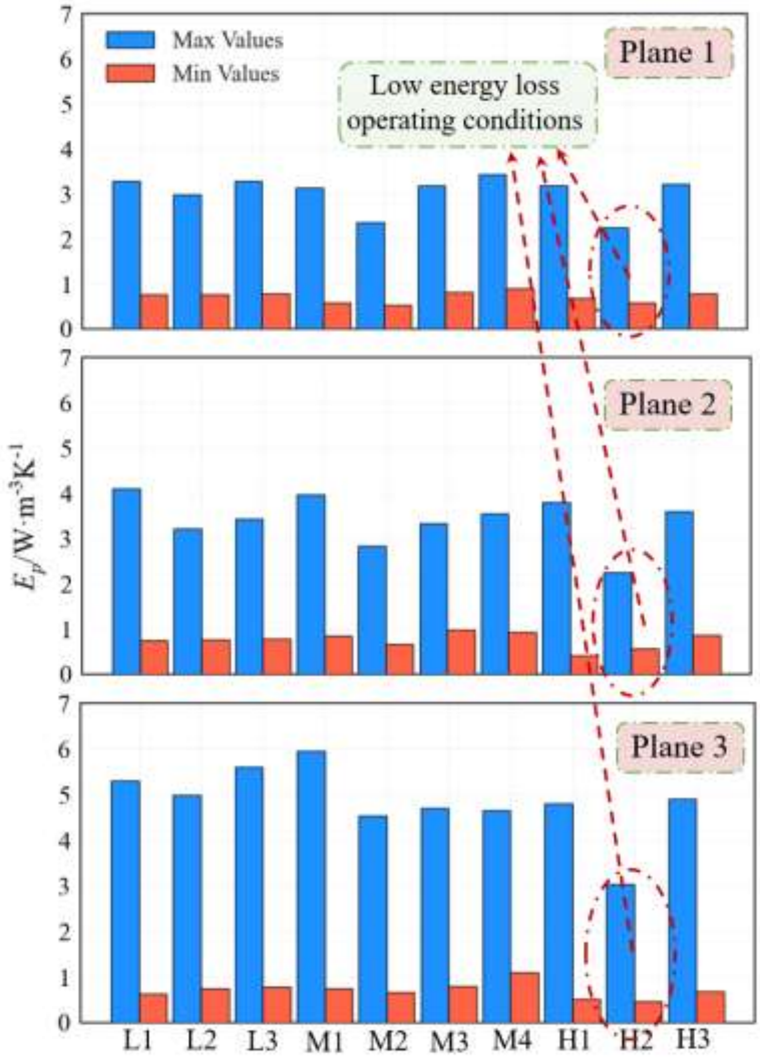

Figure 9: Distribution patterns of maximum and minimum Ep values under different operating conditions in three monitoring planes

Figure 10 presents a comparison of the Ep distribution within the draft tube flow planes under three typical high energy loss operating conditions. From the figure, it can be observed that, under the same scale, Ep shows a significant increasing trend as the relative position increases. The increase from 12m to 14m is greater than that from 10m to 12m, indicating that the energy loss degree within the draft tube gradually increases. Within the same plane, the central region is the core area of fluid flow. This region, being far from the draft tube wall, has a relatively low entropy generation value, resulting in smaller energy losses. As the flow approaches the wall, the entropy generation gradually increases, and flow losses intensify. This is primarily due to fluid impact with the wall, which causes significant velocity variations, leading to localized turbulence and unit vibrations, thereby causing additional energy loss and increasing entropy generation. In terms of relative entropy generation, the maximum entropy generation value for the L3 condition exceeds 5.5, which is higher than the other two operating conditions. This result is consistent with the analysis of the pressure pulsation percentage. Therefore, during turbine operation, it is important to promptly adjust and optimize the operating conditions of the turbine, avoiding prolonged operation under the blade 0°-guide vane 37° matching configuration.

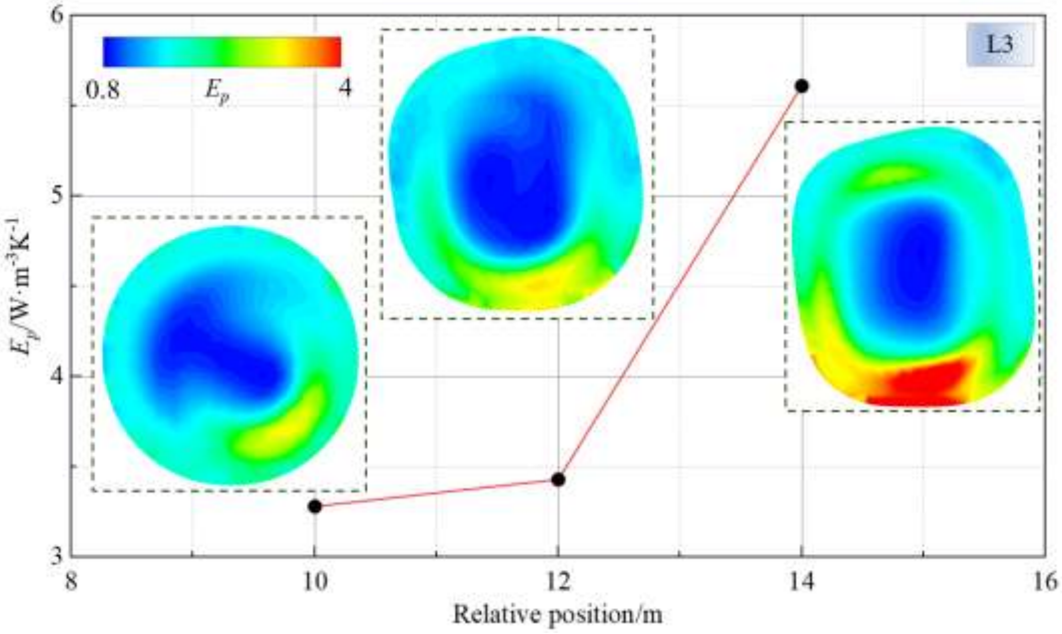

(a): L3 (blade 0 °- guide vane37 °)

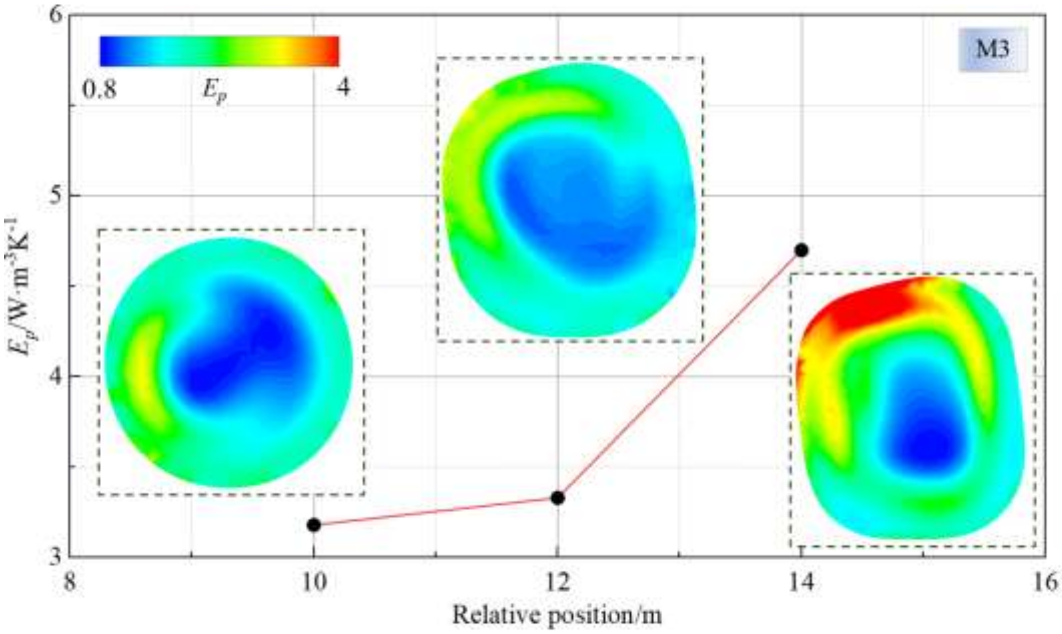

(b): M3 (blade 0 °- guide vane 29 °)

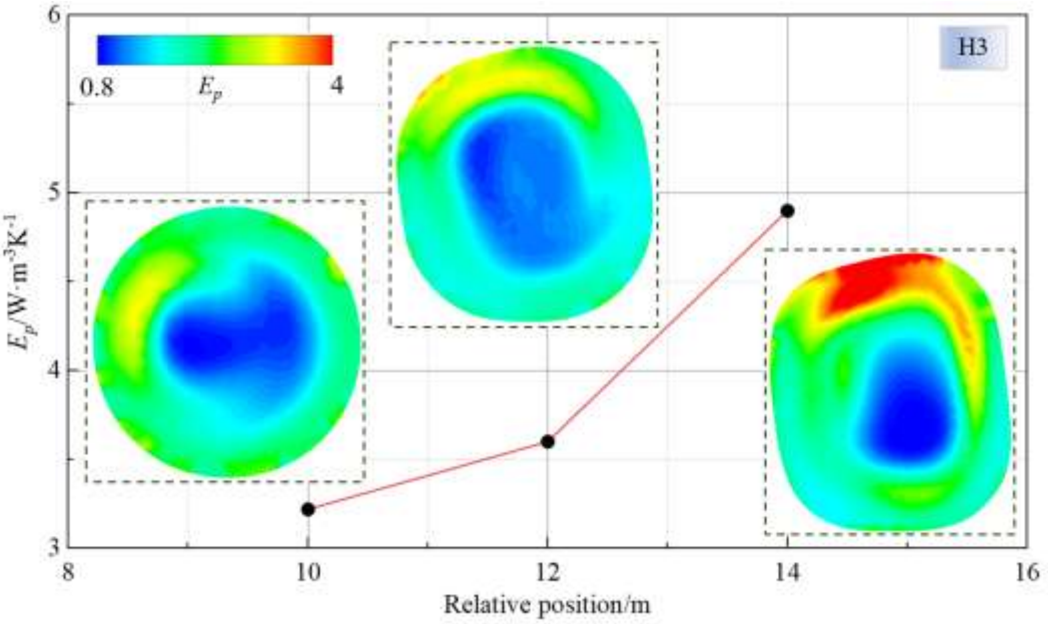

(c): H3 (blade 0 °- guide vane26 °)

Figure 10: Comparison of changes in E_p distribution along the flow direction under the same operating conditions

4.3 Time Frequency Characteristics of Pressure Pulsation

Entropy generation is a crucial quantitative indicator of energy loss in fluid flow, and pressure pulsation is an important physical source contributing to the increase in entropy generation. Therefore, a detailed analysis of the time-domain distribution of pressure pulsations and corresponding frequency domain characteristics at key locations in the turbine under different operating conditions is necessary to reveal the variation in pressure pulsation amplitude and how different frequency components affect the turbine's energy loss mechanism. Figures 11(a)-(c) show the time-domain pressure pulsation distribution and corresponding frequency distribution results for 10 typical operating points. From the figures, it can be observed that the pressure signals at all monitoring points exhibit some fluctuation, indicating the presence of significant pulsations in the flow field. At each point, the corresponding frequencies are dominated by low-frequency pulsations, with a frequency of f_c = 0.06. The next highest frequency is f_c = 5.7, which is close to the number of blades and related to the blade passing frequency (BPF), indicating that the periodic motion of the blades generates noticeable pressure pulsations at this location. In the frequency domain plots for the M2 and H1 conditions, third-order harmonics appear, with frequencies f_c = 16 and f_c = 11.5. This suggests that under the guide vane and runner blade matching conditions for these two operating points, secondary backflows or large-scale stalled vortex phenomena occur within the turbine. The propagation frequency of these stalled vortices gives rise to these specific frequencies, which in turn leads to an increase in entropy generation in certain regions.

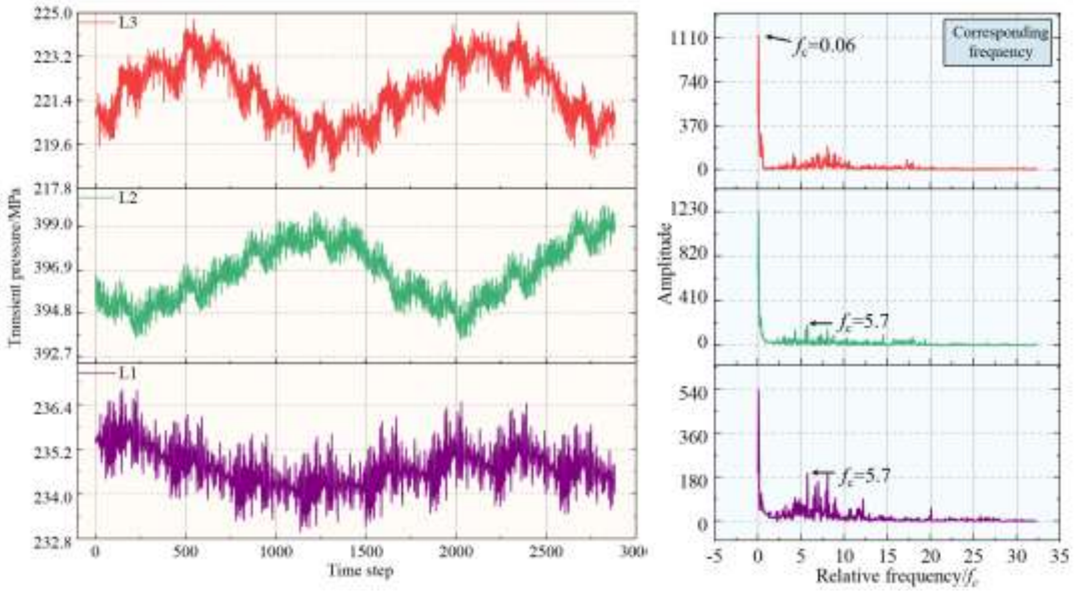

(a) Left: L1-L3 pressure pulsation time domain diagram Right: L1-L3 pressure pulsation frequency domain diagram

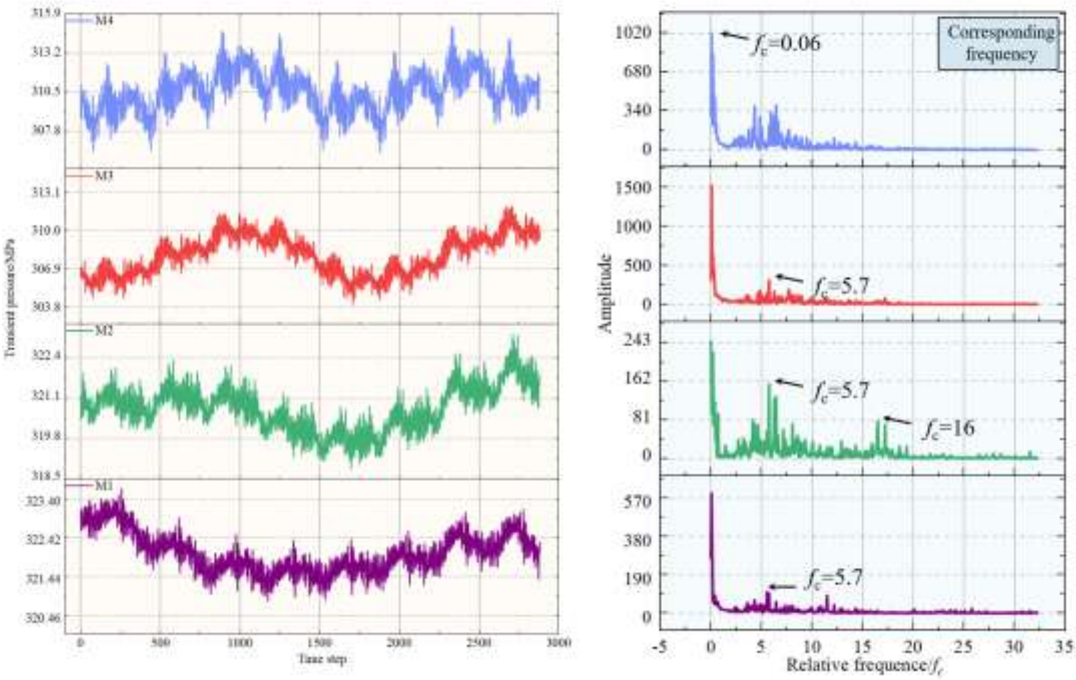

(b) Left: M1-M4 pressure pulsation time domain diagram Right: M1-M4 pressure pulsation frequency domain diagram

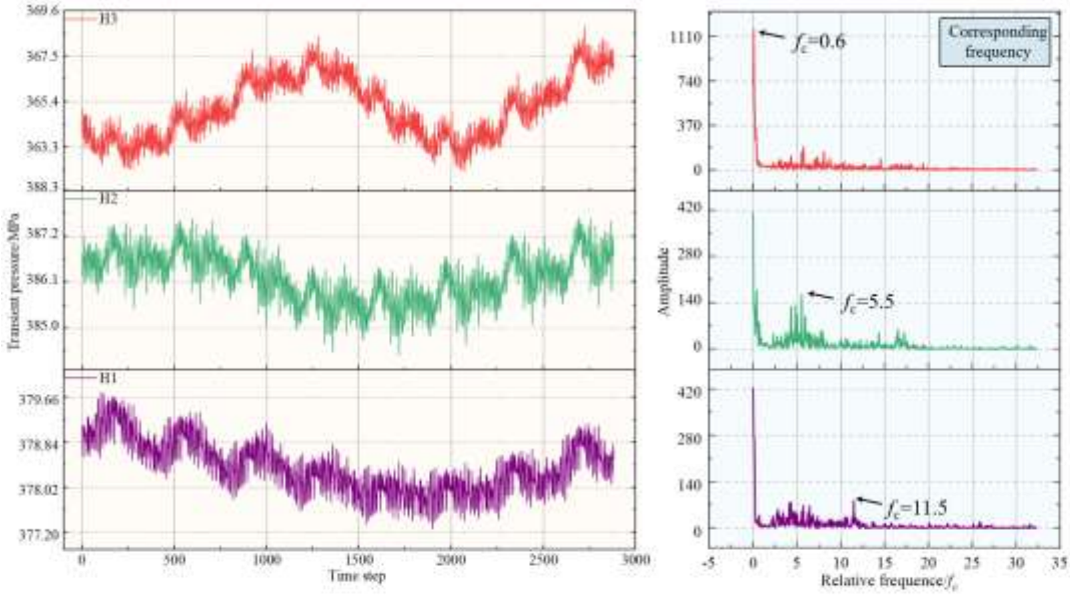

(c) Left: H1-H3 pressure pulsation time domain diagram Right: H1-H3 pressure pulsation frequency domain diagram

Figure 11: Comparison of time-frequency patterns of pressure pulsation at different operating points under different heads

4.4 Analysis of the Spatial Propagation Law of Pressure Pulsation

By analyzing the time-frequency characteristics of pressure pulsations, the characteristics of pressure pulsation signals at individual monitoring points can be obtained. However, the frequency and phase distribution patterns of pressure pulsations across a particular plane cannot be determined. Therefore, in this section, three operating conditions—L3, M3, and H3—are selected, and the amplitude, peak-to-peak value, and phase distribution of pressure pulsations at three draft tube cross-sections are analyzed. This analysis helps to understand the propagation of pressure pulsations within the draft tube and further guides the division of the operating regions of axial-flow Kaplan turbine. Figures 12(a)-(c) show the spatial propagation characteristics of pressure pulsations within the draft tube under the three conditions. From Figure 12(a), the amplitude and peak-to-peak value of pressure pulsations are lower in the central region of the draft tube. As the distance from the center increases toward the draft tube wall, both the amplitude and peak-to-peak value increase. Notably, the pressure pulsation amplitude is relatively high only in a small portion of the region, while the peak-to-peak value remains high around the entire perimeter. This is primarily due to the motion of the cavitation vortex belt in the central region of the draft tube, and the scale of the cavitation vortex belt gradually expands as the water flows within the draft tube. Regarding phase propagation, it is evident that from Plane 1 to Plane 3, the distribution area of pressure pulsations rotates clockwise by approximately π/2. In Figure 12(b), it can be observed that the spatial propagation characteristics of pressure pulsations at the draft tube cross-section under M3 are like those under L3. In Figure 12(c), under the H3 condition, the phase distribution of pressure pulsations in the three planes differs significantly from the other two conditions. This is mainly reflected in the number of phase boundary interfaces between π and -π. Under L3 and M3 conditions, there is only one such boundary, whereas under H3, there are two, and the phase characteristics along the boundary lines exhibit a mirror-image distribution. This indicates that under the H3 operating condition, the phase variation of pressure pulsations is more pronounced, and there are considerable differences in the pressure pulsation characteristics across different regions.

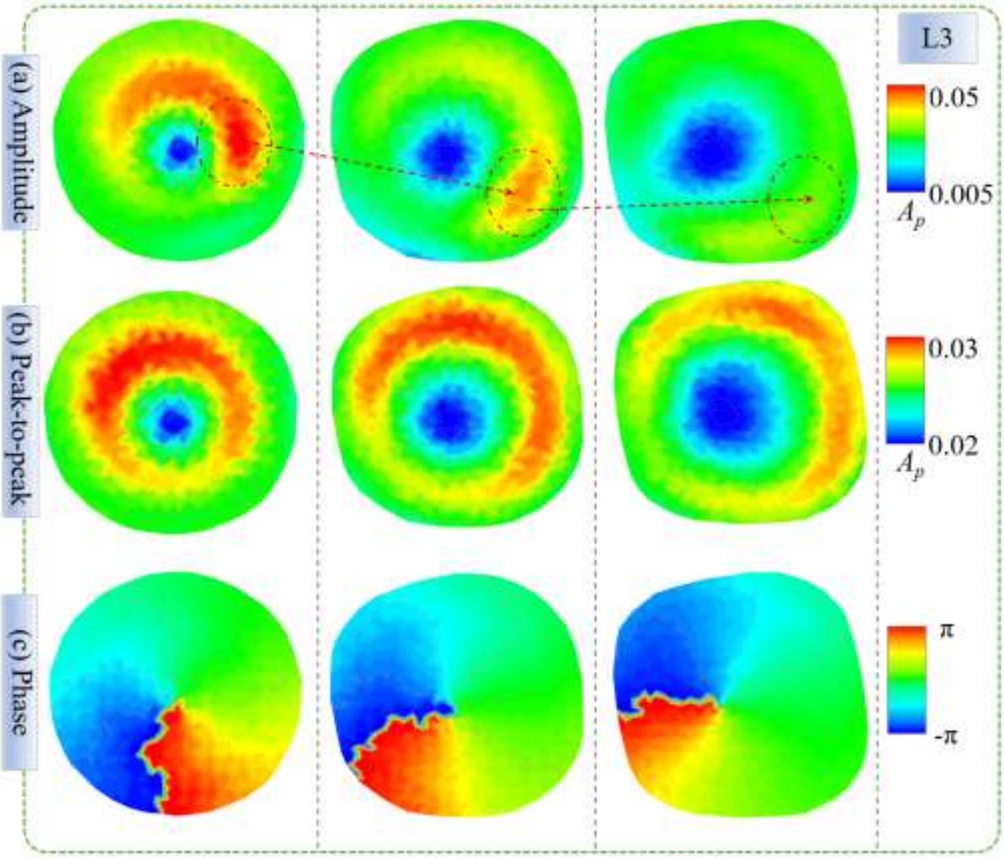

(a) The spatial propagation characteristics of pressure pulsation inside the draft tube under L3 operating conditions

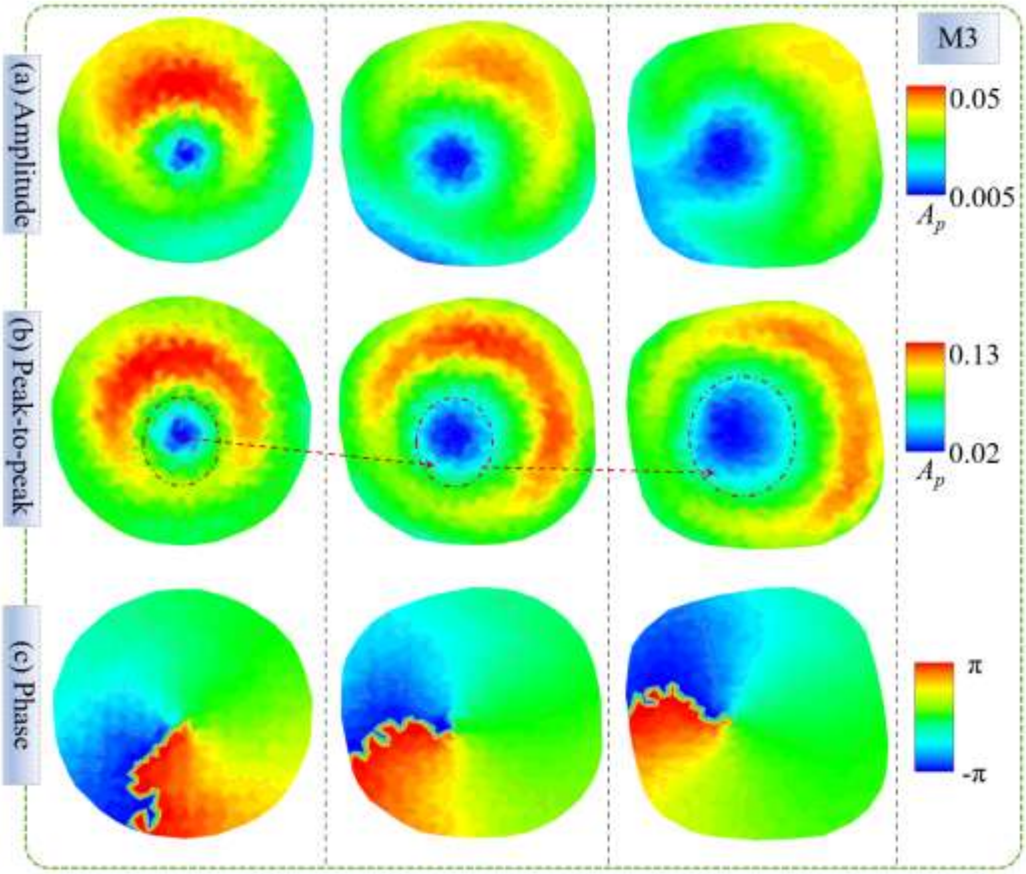

(b) The spatial propagation characteristics of pressure pulsation inside the draft tube under M3 operating conditions

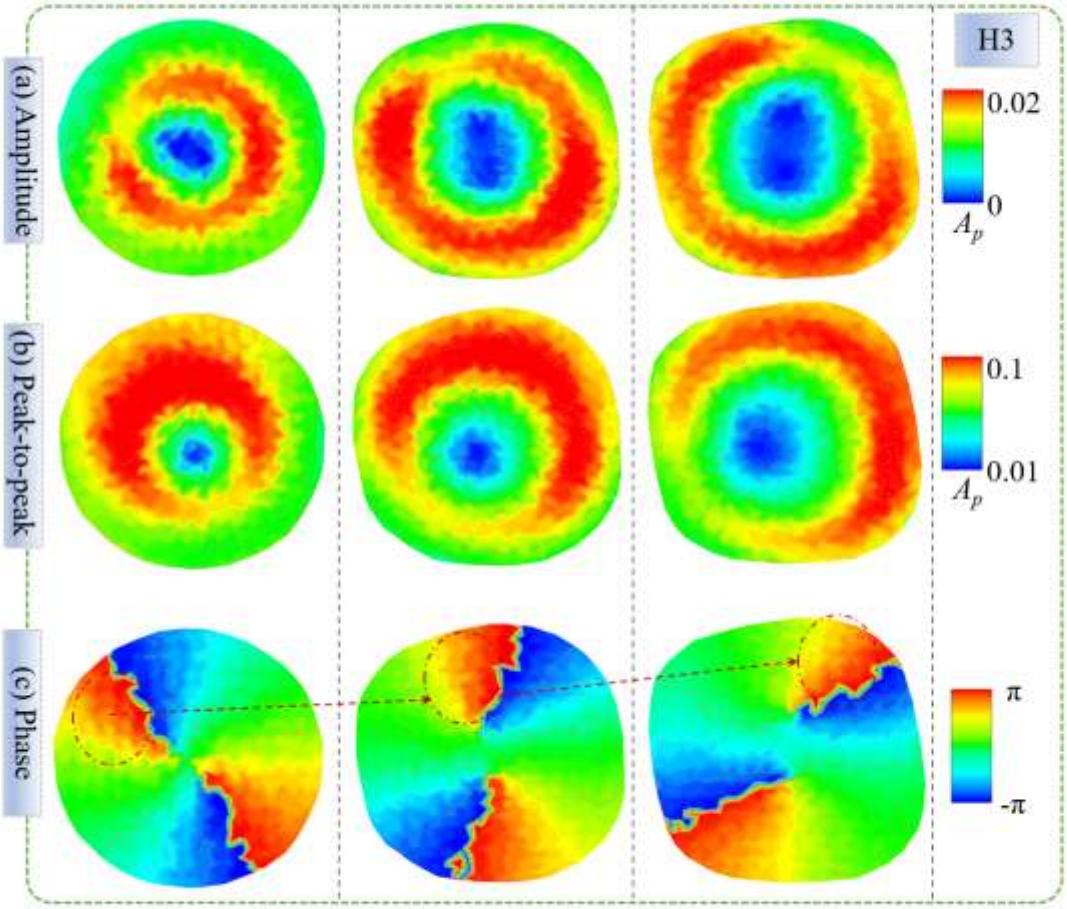

(c) The spatial propagation characteristics of pressure pulsation inside the draft tube under H3 operating conditions

Figure 12: The spatial propagation characteristics of pressure pulsations under different operating conditions inside the draft tube

4.5 Suggestions for the Operation of Axial-Flow Kaplan Turbine

In the operation of axial-flow Kaplan turbine, pressure pulsation intensity and efficiency are two critical performance indicators. Pressure pulsation intensity reflects the stability of equipment during operation, and Section 4.2 has already provided a detailed analysis of the pressure pulsation characteristics at ten typical operating points. On the other hand, the efficiency of the axial flow Kaplan Turbine unit reflects its energy conversion efficiency under various operating conditions, directly impacting the effectiveness of power generation. Therefore, different operating points exhibit different characteristics. Some operating regions show high efficiency and low pulsation, representing "high-quality" operational states, while other points display low efficiency and high pulsation, indicating "low-quality" states. Traditional classification methods typically focus on one performance aspect at a time and fail to address both aspects comprehensively, making it difficult to accurately divide the operating zones of the axial flow Kaplan Turbine. To solve this, the paper proposes the TOZ-DBSCAN, which is used for classification and partitioning of operating points and regions. This algorithm is based on the classic DBSCAN clustering method but incorporates the specific characteristics of the axial flow Kaplan Turbine operating environment. It dynamically adjusts the density sensitivity to classify different operating regions effectively. This method provides a more nuanced and accurate approach to determining the zones where the turbine operates most efficiently, based on both pressure pulsation and efficiency, ensuring a more optimal operational division.

Figure 13 shows the clustering analysis results of monitoring points at different operating positions of the axial flow Kaplan Turbine, labeled P1-P4. The horizontal axis represents the pressure pulsation percentage, and the vertical axis represents the operating efficiency of the unit.

Based on the operational results of different working conditions, the operating points are divided into two clusters: Cluster 1 and Cluster 2, representing different axial flow Kaplan Turbine operating modes. Cluster 1 represents the "high-quality" operating state with high efficiency and low pulsation, while Cluster 2 represents the "low-quality" operating state with low efficiency and high pulsation. From the figure, it can be observed that the classification results of different operating points vary depending on the pressure pulsation percentage at different monitoring points. When the pressure pulsation intensity is relatively low, such as at the turbine casing and blade-free areas, all operating points are classified as "high-quality" operating points. However, when the pressure pulsation intensity is relatively high, such as at the draft tube position, the unit operates in a "low-quality" state with low efficiency and high pulsation. During operation, the axial flow Kaplan Turbine should avoid running under the corresponding blade-guide vane combinations that lead to this low-efficiency, high-pulsation condition.

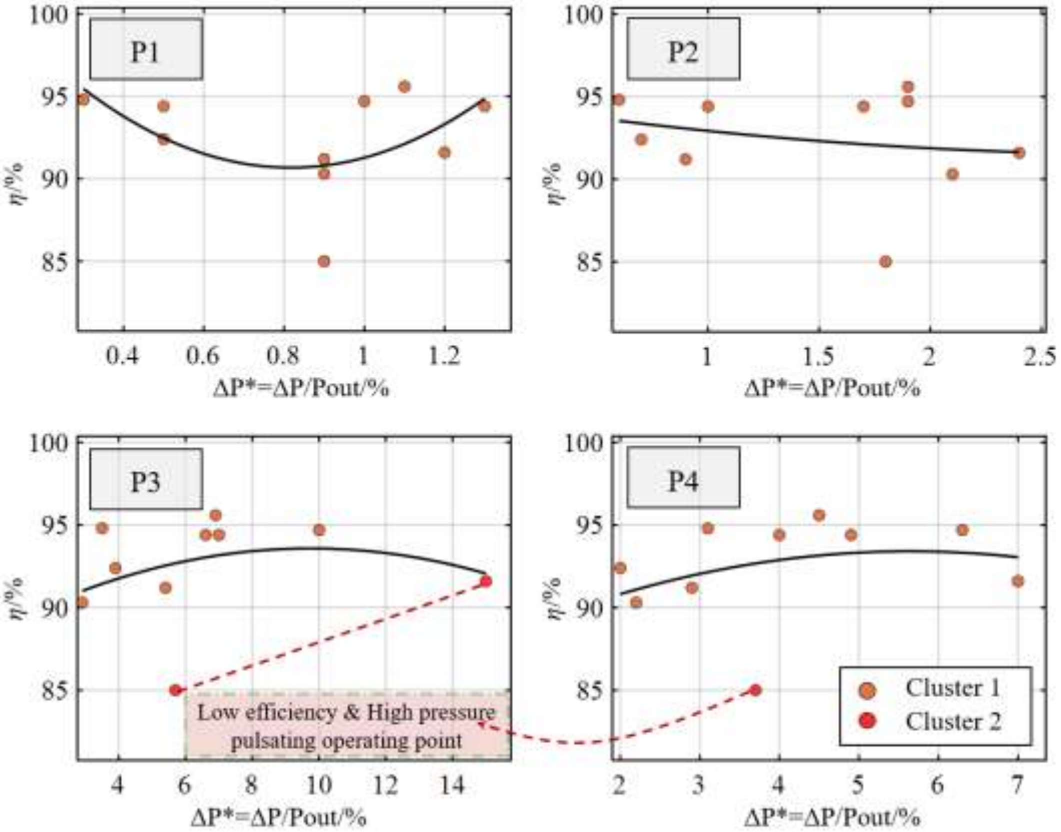

Figure 13: Clustering results of operating conditions at different monitoring points

Based on the numerical simulation results of ten typical operating conditions in different operational regions of the axial-flow Kaplan turbine, combined with the analysis of pressure pulsation percentage and entropy generation distribution patterns, the entire turbine operating region is divided. Figure 14 presents the final division results. From the figure, it can be observed that in terms of pressure pulsation percentage, the different colored grid areas represent the approximate ranges of pressure pulsation percentages in different operating regions, with blue indicating low pressure pulsation regions and purple indicating high pressure pulsation regions. In the entropy generation analysis, the "Low Energy Loss Operating Area" is highlighted, representing an ideal operating region. This region corresponds to the optimal operating range for the turbine, where the energy loss is minimized while ensuring the unit efficiency remains within a higher range. The results of this study can provide important references for optimizing operating strategies and maintenance decisions for axial-flow Kaplan turbine.

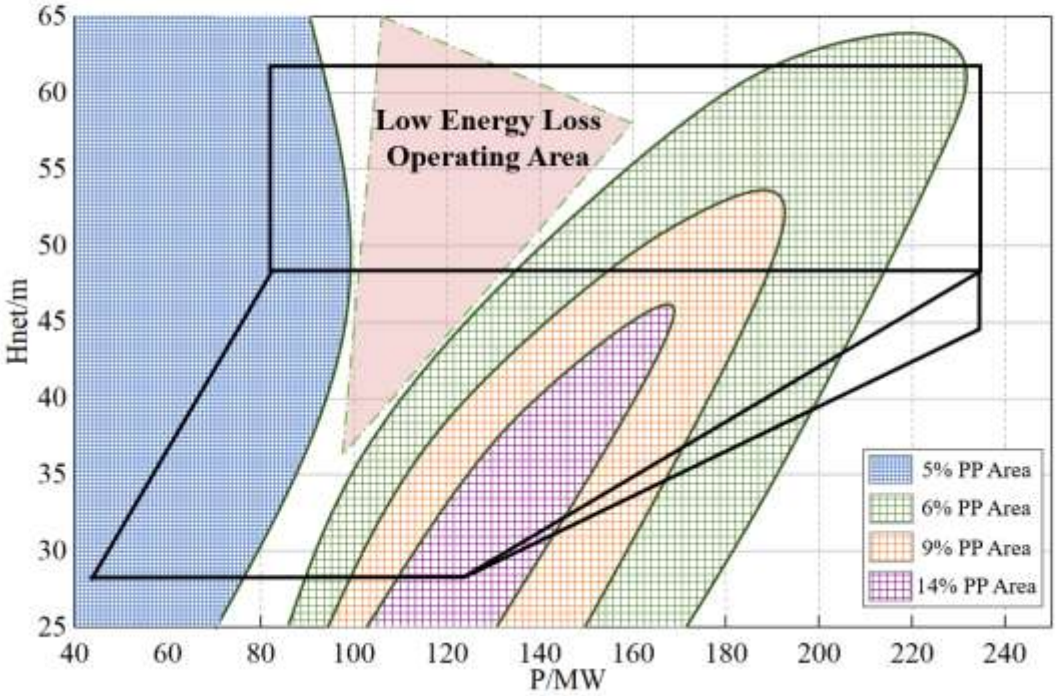

Figure 14: Results of dividing the operating area of the turbine based on pressure pulsation and entropy production analysis

5 Conclusions

This study systematically combines entropy generation theory with the pressure PTN method to reveal the energy loss characteristics and pressure pulsation propagation laws under different blade-guide vane combination conditions in axial-flow Kaplan turbine operations. A turbine operating zone density clustering algorithm is proposed, using pressure pulsation intensity and unit efficiency as criteria to classify the operating conditions of the axial-flow Kaplan turbine. The main findings are summarized as follows:

(1) The variation patterns of pressure pulsation intensity under different operating conditions inside the turbine are relatively consistent, with the maximum value occurring at the first monitoring point in the draft tube. The energy loss inside the draft tube is the primary cause of the turbine's efficiency decline. Under high head conditions, the pressure pulsation intensity is lower than that under low head operating conditions. When the blade angle is 0°, the internal pressure pulsation intensity of the turbine is the highest.

(2) When the blade opening is -5°, the entropy production of the unit remains relatively stable, and the energy loss is lower. The maximum entropy production value for the H3 operating condition is relatively high. The maximum entropy production value for the L3 condition exceeds 5.5, which is higher than the other two operating conditions, aligning with the analysis results of pressure pulsation percentage. The high entropy production regions coincide with the regions of strong pressure pulsations, indicating that flow instability is positively correlated with irreversible losses in the system. It is recommended to avoid prolonged operation under the blade 0° - guide vane 37° guide vane and runner blade matching condition.

(3) The blade passing frequency, f_c = 5.7, dominates the pressure pulsations, while high-frequency components, such as f_c = 16, are present in some operating conditions. The pressure pulsation amplitude and peak-to-peak values are lower in the central region of the draft tube and increase as the flow approaches the pipe walls. Using the TOZ-DBSCAN, operating points with poor performance characteristics are accurately identified. Additionally, based on the analysis of pressure pulsations and entropy production, the operating regions of the turbine are precisely divided. The findings of this study can provide valuable reference for optimizing unit scheduling strategies and improving the intelligent regulation capabilities of the turbine unit.

Data Availability

The datasets generated during and/or analyzed during the current study are available on request from the corresponding author.

Conflicts of Interest

The authors declare that they have no conflicts of interest.

Acknowledgements

This study is Supported by the Technology Program of State Grid Fujian Electric Power Co., Ltd.; Program Title: Research on reliability technology of key components of large capacity Kaplan turbine; Grant Number: 52130424000A. The authors would like to acknowledge the financial support of Independent Innovation Research Fund Project of China Agricultural University, Grant Number: 15054011.

CRediT authorship contribution statement

Mingkun Fang: Writing – original draft; Formal analysis. **Houyu Zhang:** Methodology; Software. **Yunshui Peng:** Resources. **Jinfu Lin:** Supervision. **Yingbo Guan:** Visualization. **Ran Tao:** Validation; Writing – review & editing. **Di Zhu:** Investigation. **Ruofu Xiao:** Funding acquisition.

References:

1. Liao J X, Liu X Y, Zhou X Y, Tursunova N R. Analyzing the role of renewable energy transition and industrialization on ecological sustainability: Can green innovation matter in OECD countries[J]. RENEWABLE ENERGY , 2023,204:141-151.
2. Chien F S, Chau K Y, Sadiq M. The effect of energy transition technologies on greenhouse gas emissions: New evidence from ASEAN countries[J]. SUSTAINABLE ENERGY TECHNOLOGIES AND ASSESSMENTS, 2023,58.
3. Chien F S, Vu T L, Phan T, Nguyen S V, Anh N, Ngo T Q. Zero-carbon energy transition in ASEAN countries: The role of carbon finance, carbon taxes, and sustainable energy technologies[J]. RENEWABLE ENERGY, 2023,212:561-569.
4. Chou J M, Li Y M, Xu Y, Zhao W X, Li J N, Hao Y D. Carbon dioxide emission characteristics and peak trend analysis of countries along the Belt and Road[J]. ENVIRONMENTAL SCIENCE AND POLLUTION RESEARCH, 2023,30(34):81881-81895.
5. Shrestha A, Mustafa A A, Htike M M, You V, Kakinaka M. Evolution of energy mix in emerging countries: Modern renewable energy, traditional renewable energy, and non-renewable energy[J]. RENEWABLE ENERGY, 2022,199:419-432.
6. Olabi A G, Abdelkareem M A. Renewable energy and climate change[J]. RENEWABLE & SUSTAINABLE ENERGY REVIEWS, 2022,158.
7. Nautiyal H, Goel V. Sustainability assessment of hydropower projects[J]. JOURNAL OF CLEANER PRODUCTION, 2020,265.
8. Sun X S, Wang X G, Liu L P, Fu R Z. Development and present situation of hydropower in China[J]. WATER POLICY, 2019,21(3):565-581.
9. Xiao L, Wang J, Wang B L, Jiang H. China's Hydropower Resources and Development[J]. SUSTAINABILITY, 2023,15(5).
10. Polák M. A Brief History of the Kaplan Turbine Invention[J]. ENERGIES, 2021,14 (19).
11. Yan D D, Luo H Q, Zhao W Q, Wu Y B, Zhou L J, Fan X F, Wang Z W. Inner Flow Analysis of Kaplan Turbine under Off-Cam Conditions[J]. ENERGIES, 2024,17(11).
12. Wei P, Li S Y. Stochastic dynamic analysis of a Kaplan turbine system considering synergistic regulation[J]. MODERN PHYSICS LETTERS B, 2021,35(15).
13. Wei P, Li S Y. Sensitivity and stability analysis of a Kaplan turbine system considering synergistic regulation[J]. NONLINEAR DYNAMICS, 2021,103(1): 383-397.
14. Deng S, Zhao W Q, Huang T B, Xia M, Wang Z W. A Comparative Study on the Cam Relationship for the Optimal Vibration and Efficiency of a Kaplan Turbine[J]. JOURNAL OF MARINE SCIENCE AND ENGINEERING, 2024,12(2).
15. Bozic I, Benisek M. An improved formula for determination of secondary energy losses in the runner of Kaplan turbine[J]. RENEWABLE ENERGY, 2016,94:537-546.
16. Luo Y Y, Yang G D, Cao J W, Yang J W, Chen J, Zhao H Y, Wang Z W. Multibody dynamics analysis of a Kaplan turbine runner

in full operating conditions[J]. JOURNAL OF ENERGY STORAGE, 2023,72.

17. Yang C X, Wu J W, Xu D E, Zheng Y, Hu X Y, Long Z. Analysis of Flow Field Characteristics and Pressure Pulsation in Horizontal Axis Double-Runner Francis Turbine[J]. WATER, 2021,13(19).
18. Wang W J, Tai G Y, Shen J W, Pei J, Yuan S Q. Experimental investigation on pressure fluctuation characteristics of a mixed-flow pump as turbine at turbine and runaway conditions[J]. JOURNAL OF ENERGY STORAGE, 2022,55.
19. Yang F, Li Z B, Yuan Y, Lin Z K, Zhou G X, Ji Q W. Study on vortex flow and pressure fluctuation in dustpan-shaped conduit of a low head axial-flow pump as turbine[J]. RENEWABLE ENERGY, 2022,196:856-869.
20. He X H, Zhao Z G, Hu J H, Yang J D, Yang J B, Peng T. Pressure fluctuation characteristics of a pump turbine in a draft tube: New insight into water column separation[J]. PHYSICS OF FLUIDS, 2022,34(9).
21. Liu C M, Chen T, Kang W Z, Kang J J, Zhou L J, Tao R, Wang Z W. Study on Pressure Pulsation and Force Characteristics of Kaplan Turbine[J]. WATER, 2023,15(13).
22. Zhang F F, Xiao R F, Zhu D, Liu W C, Tao R. Pressure pulsation reduction in the draft tube of pump turbine in turbine mode based on optimization design of runner blade trailing edge profile[J]. JOURNAL OF ENERGY STORAGE, 2023,59.
23. He X H, Yang J D, Yang J B, Zhao Z G, Hu J H, Peng T. Evolution mechanism of water column separation in pump turbine: Model and occurrence criterion[J]. ENERGY, 2023, 265.
24. Roh C, Kim K H. Deep Learning Prediction for Rotational Speed of Turbine in Oscillating Water Column-Type Wave Energy Converter [J]. ENERGIES, 2022,15(2).
25. Liu X L, Tian Y, Lei X H, Liu M, Wen X, Huang H C, Wang H. Deep forest based intelligent fault diagnosis of hydraulic turbine[J]. JOURNAL OF MECHANICAL SCIENCE AND TECHNOLOGY, 2019,33(5) :2049-2058.
26. Pan H, Hang C Y, Feng F, Zheng Y, Li F. Improved Neural Network Algorithm Based Flow Characteristic Curve Fitting for Hydraulic Turbines[J]. SUSTAINABILITY, 2022,14(17).
27. Xu J, Wang L Y, Yuan J P, Luo Z H, Wang Z L, Zhang B W, Tan A. DLFSI: A deep learning static fluid-structure interaction model for hydrodynamic-structural optimization of composite tidal turbine blade [J]. RENEWABLE ENERGY, 2024,224.
28. Xiong L, Liu J J, Song B, Dang J, Yang F, Lin H K. Deep learning compound trend prediction model for hydraulic turbine time series[J]. INTERNATIONAL JOURNAL OF LOW-CARBON TECHNOLOGIES, 2021,16 (3):725-731.
29. Korkos P, Kleemola J, Linjama M, Lehtovaara A. Representation Learning for Detecting the Faults in a Wind Turbine Hydraulic Pitch System Using Deep Learning[J]. ENERGIES, 2022,15(24).
30. Masood Z, Khan S, Qian L. Machine learning-based surrogate model for accelerating simulation-driven optimisation of hydropower Kaplan turbine[J]. RENEWABLE ENERGY, 2021,173:827-848
31. Celik, I.B., Ghia, U., et al. Procedure for Estimation and Reporting of Uncertainty Due to Discretization in Cfd Applications. JOURNAL OF FLUIDS ENGINEERING-TRANSACTIONS OF THE ASME, 2008(7)
32. MENTER, F.R. 2-Equation Eddy-Viscosity Turbulence Models for Engineering Applications. AIAA JOURNAL, 1994(8): 159 8-1605
33. Menter, F.R. Review of the Shear-Stress Transport Turbulence Model Experience From an Industrial Perspective. INTERNATIONAL JOURNAL OF COMPUTATIONAL FLUID DYNAMICS, 2009(4): 305-316.